Molecular Dynamics Simulations of Cascade Evolution near Pre-Existing Defects

A Thesis Presented for the

Master of Science

Degree

The University of Tennessee, Knoxville

Nathan Allen Capps

December 2013

Abstract

Radiation damage causes significant changes to material microstructure and properties as a result of the processes of atomic defect creation followed by the inherently multiscale evolution by defect diffusion and reactions. In particular, the overlap of displacement cascades is believed important in the development of visible defect clusters in thin film, *in situ* ion irradiation studies. In this work, we use molecular dynamics simulations to investigate how impurities and damage induced by displacement cascades impact damage creation as well as the mobility of a pre-existing interstitial-type dislocation loop in BCC iron. It is well known that impurities, such as oxygen, carbon, and nitrogen impact the mobility of interstitial dislocation loops, and are likely responsible for the difference in loop diffusivities between computer simulations and experimental observations by transmission electron microscopy. We have used molecular dynamics simulations to evaluate whether a displacement cascade could de-trap an interstitial cluster from interstitial impurity atoms. By varying the energy and directional velocity of the primary knock on atom (PKA), we observe how the trapped defect reacts with the cascade damage. Our simulation results reveal that cascades with PKA energy greater than 10 keV can cause the loop to de-trap from impurities, but the loop often rapidly becomes trapped in the cascade debris. Furthermore, on several occasions, the cascade induces a change in orientation, or Burgers vector, in addition to modifying the size of the dislocation loop. This thesis summarizes the molecular dynamics simulation results as a function of PKA energy, as well as the effect of loop size, in terms of the probability for de-trapping and subsequent diffusion. Furthermore, molecular dynamics simulations results will be presented that quantify on the impact of pre-existing vacancies on defect production as a function of PKA energy and concentration. These simulation results provide a basis to inform cluster dynamics models of dislocation loop evolution in irradiated ferritic/martensitic alloys.

Table of Contents

Chapter 1: Introduction…….....1

1.1: Experimental Observations Compared to Molecular Dynamics Predictions……...1

Chapter 2: Research Approach/Computational Method……10

2.1: Molecular Dynamics……10

2.2: Large-Scale Atomic/Molecular Massively Parallel Simulator(LAMMPS)…….12

2.3: Interatomic Potentials……..14

Chapter 3: Cascade-Loop Interaction……17

3.1: Methodology……....18

3.2: Results…….……20

Chapter 4: Pre-existing Vacancies Affect on Defect Production…….....……....26

Chapter 5: Summary and Outstanding Issues……....33

List of References……..34

Vita…….36

List of Tables

Table 3.1 Simulation system size……..……..20
Table 3.2 Quantification of the impact of displacement cascades ……..24
Table 3.3 Quantification of the impact of displacement cascades on defect production...25
Table 4.1 Impact of voids on defect production……27
Table 4.2 Influence of the number of pre-existing vacancies on defect production……..29

List of Figures

Figure 1.1 Images of successive ion fluence increments in Fe-8%Cr irradiated…….2
Figure 1.2 Positron annihilation spectroscopy (PAS) measurement ……..3
Figure 1.3 Comparison of the number of surviving Frenkel ……..5
Figure 1.4 The fraction of self-interstitial atoms contained within a cluster ……..5
Figure 1.5 The fraction of vacancies within a cluster ……6
Figure 1.6 Relationship of the motion frequency of interstitial dislocation loops ……..8
Figure 2.1 Flow chart describing the logic for a molecular dynamics simulation ……11
Figure 2.2 LAMMPS parallel efficiency ……..13
Figure 2.3 Linear relationship between simulation time and walk clock time …….14
Figure 2.4 Schematic illustration of Lennard-Jones potential……...15
Figure 2.5 Plot of Potential energy versus separation distance ……17
Figure 3.1 Diffusivity of a 91 member dislocation loop ……...18
Figure 3.2 Evolution of a 10 keV cascade near a trapped dislocation loop……...20
Figure 3.3 Evolution of a 5 keV cascade near a trapped dislocation loop…….21
Figure 3.4 Snapshots in time from a 10 keV simulation ……...23
Figure 4.1 Evolution of a 10 keV cascade near a void …….26
Figure 4.2 Effect of pre-existing vacancies on defect production…….30
Figure 4.3 Self-Interstitial clustering fraction……31

Chapter 1:

Introduction

1.1 Experimental Observations Compared to Molecular Dynamics Predictions

Ferritic materials are the leading candidate structural component and fuel cladding for advanced fusion and generation IV reactors, respectively. Ferritic materials are chosen for good thermal properties as well as resistance to void swelling. A significant draw back to these materials is the radiation induced hardening, which occurs at temperatures lower than 400° C [1]. The ability to study ferritic materials under the irradiation conditions expected in next generation of nuclear reactors is challenging, due to the lack of facilities that are capable of providing representative conditions that are present during irradiation. Materials in nuclear reactors are subject to fast neutron flux as well as high fluences, high temperature, and stress. All of which play a role in the evolution of the materials microstructure. To further complicate the matter, it is difficult to evaluate the effects of impurities on the mechanical properties of ferritic alloys during irradiation [2]. To fully evaluate the role that pre-existing defects and impurities play in the evolution of the materials mechanical properties, simulations of displacement cascades using molecular dynamics are need to comprehend the mechanisms that govern defect microstructural evolution.

Irradiating ferritic alloys to doses on the range of a few displacements per atom (dpa) with heavy ions produces a microstructure characterized by a growing density of small defects characterized as black dots ranging from 1-5 nanometers in diameter [3,4]. This "black dot" damage is believed to consist of interstitial-type dislocation loops which have Burgers vectors that lie in the <111> or <100> direction. The size of these transmission electron microscopy (TEM) visible features, which is on the order of nanometers, is larger than clusters produced directly by a single cascade according to MD simulations. MD predictions indicate that higher energy PKA's, on the order of 100 keV, can form stable defect clusters, containing about 20 atoms, but the majority of the interstitial clusters form smaller clusters [5]. This leads to the conclusion that the formation of visible clusters, as seen in TEM, must be results of reactions of smaller damage features from multiple cascade events. The formation of interstitial loops during electron irradiation reinforces this interpretation. The smaller loops which constitute the nuclei from which the larger ones grow will find sinks and annihilate if fully glissile, suggesting that the interactions responsible for preventing easy glide for visible loops impact smaller clusters as well.

Many *in situ* experiments have been conducted on thin iron foil samples within a TEM, using 100 keV Xe ion irradiation at lower fluence < 8e17 ions m^{-2} visible defects are not seen [7,8]. As the fluence exceeds 8e17 ions m^{-2}, visible defects in the form of black dots, which are presumed to be dislocation loops, begin to appear. The density of the dislocation loops increases along with the size of these defects. Eventually these

visible defects reach a saturation density but continue to grow in size. The evolution of visible defects as a function of fluence can be seen in Figure 1.1.

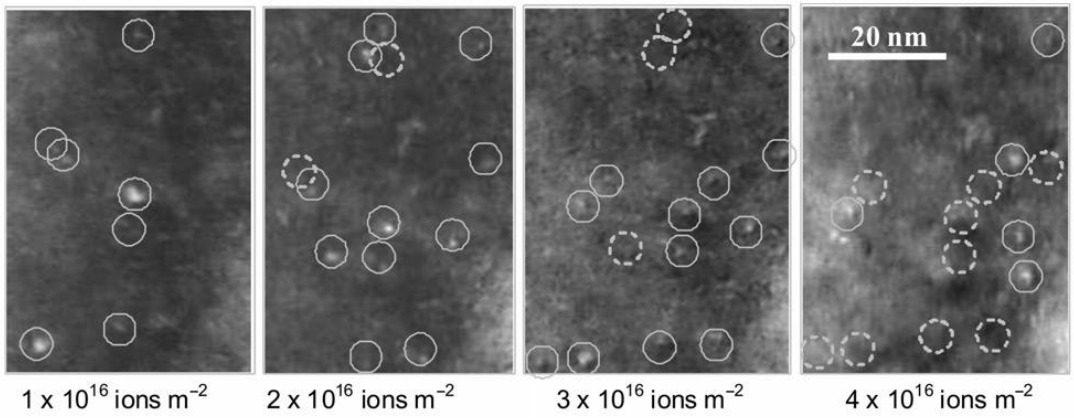


Fig. 1.1. Images of successive ion fluence increments in Fe-8%Cr irradiated with 100 keV Xe ions at room temperature, as reproduced from Yao [1]. The solid circles represent new defects and the dashed circles represent defect that have disappeared.

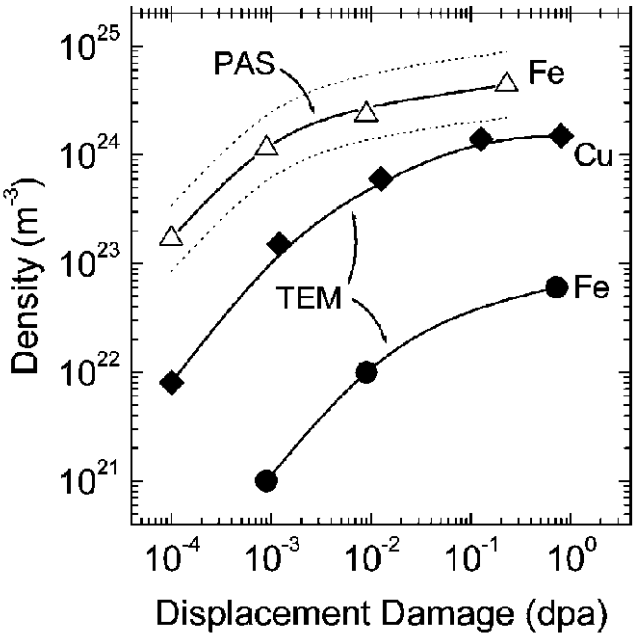


Fig 1.2. Positron annihilation spectroscopy (PAS) and transmission electron microscopy (TEM) measurement used to analysis the dose dependence on the defect cluster density in neutron irradiated iron and copper, as reproduced from reference [9]. TEM results describe the density of interstitial clusters, while the PAS results analysis the total density of vacancy clusters.

It is evident from Figure 1.1 that as the ion fluence increases the number of defects begins to saturate and start to grow in size. Furthermore, many of the visible defects in Figure 1.1 seem to appear in one of the images and then disappear in the next. This leads to the idea that the visible defect reacts with another defect. Figure 1.2, which references TEM results [9], reinforces the saturation of interstitial type dislocation loops as a function of dose. However, there are differences comparing neutron damage to ion damage. The largest difference is the time it takes to accumulate dpa. Ion irradiation is significantly faster at producing larger dpa, whereas neutron irradiation produces small dense cascades, causing an increase in the irradiation time. However, as Figure 1.1 and 1.2 show, the saturation of visible defects occurs as dose increases.

Heavy ion or neutron irradiation of materials creates energetic recoil events. The resulting primary knock-on atoms induce dense cascades of atomic displacements which occur over picosecond timescales and produce lattice defects such as monovacancies, self-interstitials, and large defect clusters [10,11]. Radiation damage experiments are able to investigate defects on the order of nanometers but are unable to determine the evolution of cascade debris to nano size defects. The initiation of defect formation begins with a high energy particle colliding with a lattice atom. This atom is defined as a primary knock on atom (PKA), which elastically collides with a secondary atom, and this

process continues till the energy is dissipated [5]. This process of creating a PKA and the dissipation of its energy to the lattice is on the order of a few picoseconds. If the energy transfer is sufficiently high, defects are created in the form of displaced atoms, called interstitials, and vacant lattice sites. The vacancy-interstitial threshold for creating a defect pair, defined to be a Frenkel pair, is referred to as the threshold displacement energy, E_d, and is 40 eV for iron [5]. Radiation damage in a material is quantified by describing how many atoms have been displaced from their lattice sites (dpa), which is used as a radiation exposure parameter. There are many models that evaluate the dpa that occurs during a high-energy particle exposure. The standard model to calculate atomic displacement rates was developed by Norgett, Robinson, and Torrens [5] and is better known as the NRT model:

$$\boldsymbol{\nu}_{NRT} = \frac{0.8T_d(E_{PKA})}{2E_d} \qquad (1)$$

Where T_d is the transferred energy from the PKA the average displacement energy of E_d, and $\boldsymbol{\nu}_{NRT}$ is the number of displaced atoms produced. The factor 0.8 takes into account atomic scattering interactions in real materials is not well described by a hard wall potential [5]. Following the peak of the cascade, ~1 picosecond after initiation of the cascade, many of the displace atoms do not remain as debris in the material, but instead the displaced atoms annihilate with vacancies left by the cascade. However, the atoms that do not annihilate with vacancies remain as cascade debris.

Due to the time scale as well as the size of small defects produced by a single cascade, molecular dynamics is ideally suited to study radiation damage at the atomistic scale. MD is discussed in detail in chapter 2. Radiation damage in iron has been thoroughly studied by Stoller and Malerba [5,12,13,14]. These studies have shown trends that describe the primary radiation damage production in iron. The first is the number of Frenkel pairs produced by an induced cascade follows a power law dependence on the energy of the PKA, as opposed to the linear dependence suggested by Eq (1). Also the clustering fraction of the surviving defects increase with increasing energy, and lastly there is a weak temperature dependence on defect production [18]. The results of these studies for lower energy cascades, 0.5-10 keV, have provided a trend for the number of defects induced within a damage cascade:

$$N_D = 5.67E_{MD}^{0.779} \qquad (2)$$

This relationship begins to deviate as the PKA energy increase and produces sub-cascades, which are present in radiation experiments [5]. However, damage production in iron has been studied thoroughly in the literature [15,16,17]. Figures 1.3-1.5 show the defect formation in iron as a function of the potential and the PKA energy [15].

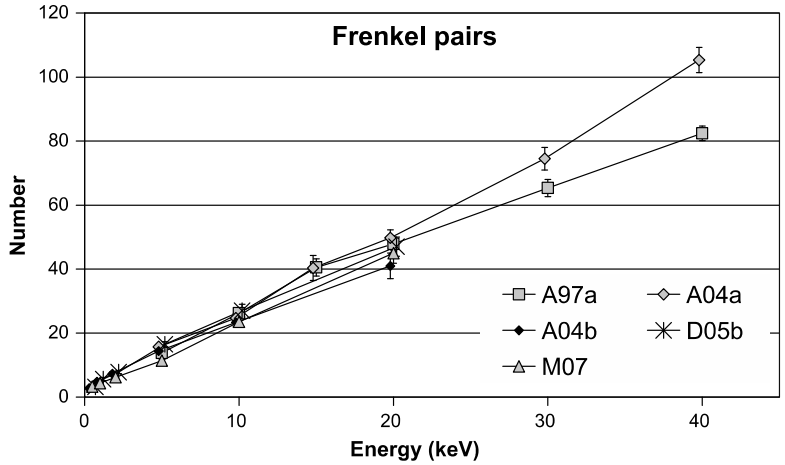


Fig 1.3. Comparison of the number of surviving Frenkel pairs produced within a damage cascade as a function of PKA energy based on different types of potentials in iron, as reproduced from ref [15].

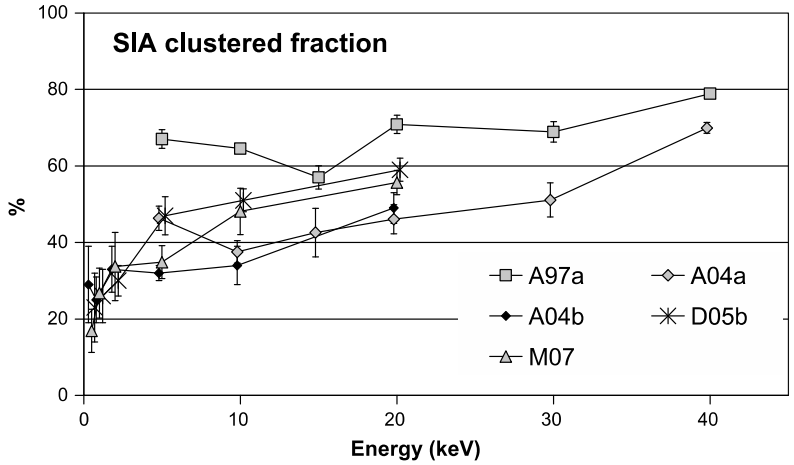


Fig 1.4. The fraction of self-interstitial atoms contained within a cluster as observed by MD cascade simulations as a function of PKA energy and interatomic potential (as reproduced from ref [15]).

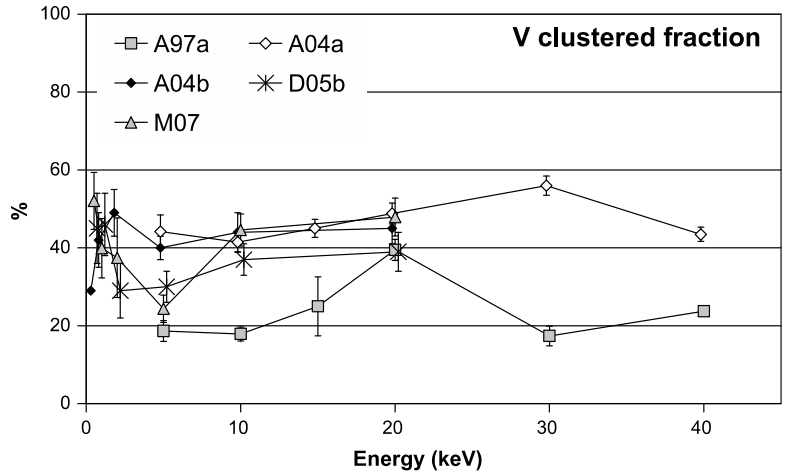


Fig 1.5. The fraction of vacancies within a cluster as observed by MD cascade simulations as a function of PKA energy and interatomic potential (as reproduced from ref [15]).

Malerba and co-workers [15] found little dependence on the number Frenkel pairs produced as a function of interatomic potential and PKA energy, as seen in Figure 1.3. However, Figures 1.4 and 1.5 show more pronounced differences between interatomic potential predictions of interstitial and vacancy clustering fractions. There are different explanations for this behavior, many of which originate from the assumptions made during potential development, but even with the difference between the clustering fractions, trends emerge as the PKA energy increase. For the interstitial clustering fraction, the interatomic potentials predict similar cluster stability as well as cluster mobility, and have similar repulsive nature [15].

MD simulations have consistently demonstrated that much of the damage produced in cascades takes the form of defect clusters rather than isolated Frenkel pairs, as seen in Figure 1.4 [12,18,19,20,21,22]. With increasing time and/or dose, these primary damage features can interact through thermal diffusion to form observable microstructural changes. Long-term damage accumulation in cascade environments is highly sensitive to the kinetic properties of both smaller and larger clusters, as demonstrated by object kinetic Monte Carlo models [23,24]. This underscores the necessity for understanding the migration and interaction properties of larger defect clusters in addition to those of single interstitials and smaller clusters, which cannot be directly experimentally measured.

Unfortunately, the long-time behavior of many of the larger clusters produced in cascades in BCC metals is poorly understood, particularly in iron. A number of complications arise from pronounced discrepancies between the mobility of dislocation loops observed in MD simulations and in experimental observations. MD computer

simulations consistently reveal that prismatic dislocation loops in pure BCC iron are observed to glide freely along the direction of their Burgers vector with activation energies below 0.1eV, regardless of their size [20,24,25,26].

Atomistic modeling studies have been conducted to determine the affect of substitutional impurities, such as Cu and Cr, on self-interstitial cluster diffusion [27,28]. These studies indicate that the diffusional pre-factor decreased as a result of the presence of substitutional Cu or Cr, as well as relatively minor changes to the activation energy for diffusion. Marian et al. actually observed slight decreases in the activation energy for SIA clusters containing between 2 and 20 SIA, with all of the activation energies being less than 0.1 eV; whereas Terentyev et al. observed an increase in the activation energy of a 7-SIA cluster with 5 or 10% Cr, but the activation energy remained quite low on the order of 0.3 eV. Experimentally, the effect of substitutional Cr in Fe-Cr alloys has been studied by Arakawa and co-workers [14]. Figure 1.6 describes these results, which assessed the frequency of interstitial-type dislocation loop motion in pure Fe versus an Fe-9Cr alloy. Figure 1.6 shows that the loops in Fe-9Cr had a lower frequency of motion as compared to the dislocation loops in pure iron [30]. Thus, both the MD simulation and experimental observations indicate relatively little influence of sutitutional solutes on SIA cluster mobility. It is important to point out however, that the affect of substitutional solutes on interstitial cluster diffusivity may be higher if the solutes are segregated to the loop periphery then if they are randomly distributed. Indeed, Arakawa et al. [14] note that Cr segregation to the loop periphery can suppress the motion of loops at temperatures above about 450 K.

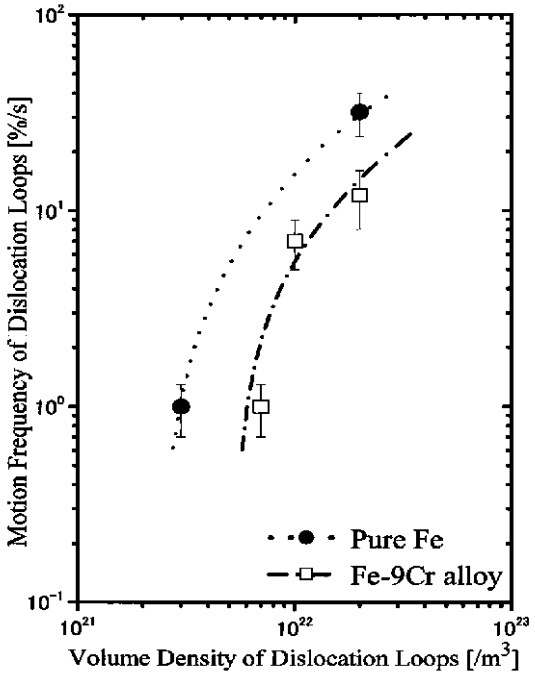


Fig 1.6. Relationship of the motion frequency of interstitial dislocation loops as a function of volume density in pure Fe and Fe-9%Cr at temperatures from 190 to 375 K, as reproduced from ref [14].

While the experimental results in Figure 1.6 show a relatively small affect of substitutional solutes on the frequency of loop motion in pure Fe versus an Fe-9%Cr alloy across the temperature range of 190 to 375 K, additional experimental investigation by Arakawa and co-workers [29] to study loop diffusion do not agree well with the MD simulations. Arakawa and co-workers performed detailed *in situ* TEM analysis of loop motion at temperatures from 526 to 667, and then compared the resulting diffusivities to that of C and N. They found that the temperature dependence of the loop motion was quite strong over this temperature range, with an activation energy of 1.3 eV, independent of loop size [29]. This value is quite different than the migration activation energy values obtained from MD simulations of less than 0.1 eV to about 0.3 eV. Thus, we conclude that the influence of interstitial type impurities on interstitial-type dislocation loop motion is a very strong affect in real materials, which must be considered in modeling the longer term behavior of dislocation loop formation and evolution.

Irradiation environments provide an additional complication regarding interstitial cluster mobility. *In situ* irradiation experiments have demonstrated a significant increase in the observed mobility of black dot damage during ion-beam exposure. Loops which are thermally immobile exhibit motions during either electron or heavy-ion irradiation best characterized as quick, infrequent hops with lengths that vary from a few to a few tens of nanometers and occur regardless of irradiation temperature [1,32]. These hops lead to further development of the defect population, and have been observed to result in

coalescence events as well as the annihilation of loops at a free surface [8]. This process presumably occurs among sub-visible loops as well. It is possible that these non-thermally activated events play a significant role in the development of visible damage, particularly in an irradiation condition where dense cascades with high ratios of large clusters dominate.

The observation of ion-beam induced mobility for interstitial clusters fits well within the context of a trap mediated diffusion environment. A trapped defect is thermally immobile, but an isolated defect is mobile at all reasonable temperatures. If a defect were to become unbound from the trapping site it would undergo free glide until encountering another trapping site. Given the low activation energy of the gliding process, this procedure would be observed as a rapid long range hop. In this scenario, the hop is initiated by a recoil event, which separates the loop from its initial trap. Experimental data showed that the frequency of these hops is directly proportional to beam flux while hop distance falls with rising impurity content [6], as one would expect based on this model. This thesis examines computationally cascade interactions with pre-existing self-interstitial dislocation loops as a mechanism for inducing loop mobility and assisting in the saturation of visible defect clusters.

Chapter 2:

Research Approach/Computational Method

2.1 Molecular Dynamics

The short-term behavior of defects at the nanometer scale is well suited for simulations by molecular dynamics, because it provides the ability to follow the atomic position, velocity, and acceleration, or atomic trajectory of an ensemble of atoms [29]. Furthermore, molecular dynamics gives the ability to study larger scales of atoms, on the order of 100 nanometers, while maintaining computational efficiency. While, first principle electronic structure calculations can predict more accurate solutions, compared to molecular dynamics, but are computational expensive to study structures on the nano-scale. Advanced experimental techniques, such as TEM have a sufficiently high resolution to observe small dislocation loops on the order of 1-5nm, but do not have the capability to resolve very small dislocation loops [3,4]. MD provides the ability to study the interactions of these small dislocation loops with the surrounding environment at the atomic scale. Figure 2.1 shows a flow chart of the individual steps related to a molecular dynamics simulation to better understand this computational technique.

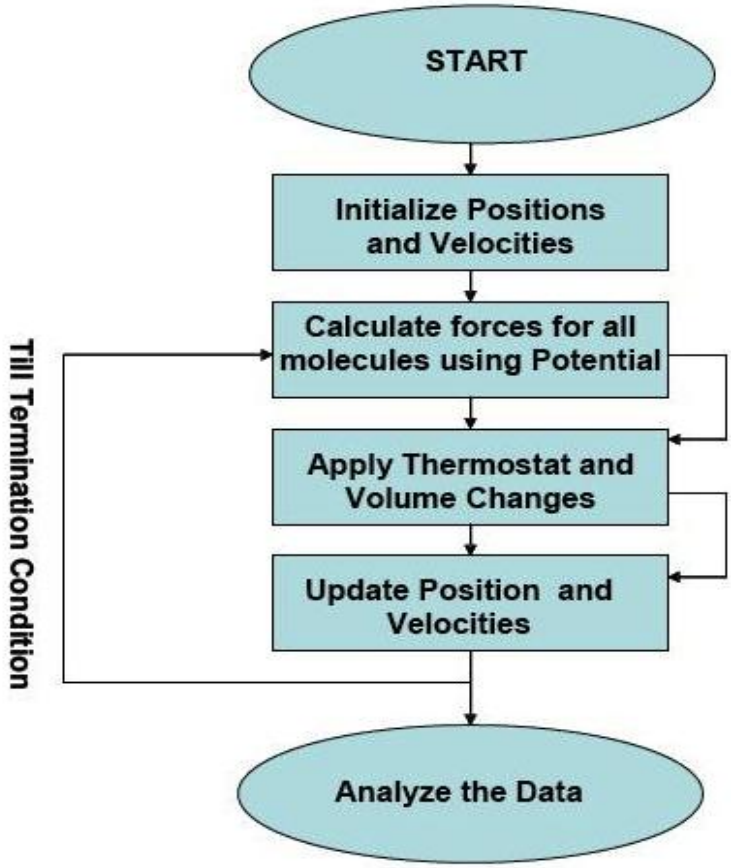


Fig. 2.1 Flow chart describing the logic for a molecular dynamics simulation.

The first step in a MD simulation, as shown in Figure 2.1, is to set up the type of atoms that will be included in the simulation, along with the initialization of the atoms position and velocities. The system size is created using a prescribed simulation cell dimension in three directions defining a polyhedron. Following the construction of the system, it is then populated by the given atoms as defined by the crystal structure, lattice parameter and atomic weight. The initial kinetic energy is given in the form of temperature, which gives initial velocities to atoms based on a random number seed. A thermostat can be applied to ensure that the system reaches the equilibrium temperature during an equilibration phase of the simulation prior to the start of the simulation of interest. The function of the thermostat is to adjust the temperature of the system based on the previous time step by increasing or decreasing the kinetic energy of the system to match the equilibrium temperature. The interactions between the atoms in the simulation are calculated for each atom according to a given interatomic potential, which will be discussed in the following section. This procedure continues until a termination condition is reached.

2.2 Large-Scale Atomic/Molecular Massively Parallel Simulator (LAMMPS)

The MD simulations described in this thesis have been performed using the LAMMPS code. LAMMPS is a molecular dynamics code that is developed and maintained at Sandia National Laboratory [30]. LAMMPS has been developed to deterministically solve Newton's equations of motions (3). Section 2.3 will describe the interatomic potential, but the governing equations of motion are:

$$F_i = m_i a_i = m_i \frac{d^2 r}{dt^2} \quad (3)$$

$$F = -\nabla U \quad (4)$$

Where F_i is the force acting on the i^{th} atom with mass m_i and acceleration a_i. ∇U is the spatial gradient in the potential energy.

The code capabilities consist of being able to model a system of atoms with varying boundary conditions, such as periodic or free surfaces, while applying varying forces in a two or three dimensional framework. For the purpose of this thesis, periodic boundary conditions were used. Periodic boundary conditions assume the system is bulk-like, and repeats itself infinitely in all directions. Furthermore, conservation of mass is simulated, no atoms are lost through the boundary of the system [30]. LAMMPS follows the atoms in the system along the entire (x,y,z) coordinate system to determine the separation of attractive and repulsive forces by the interatomic potential for each time step initiation as well as to analysis the simulation using a post processor.

LAMMPS also has the capability to perform parallel simulations for systems that are too large to run on a single processor. This parallel capability allows for a user to increase the size of the simulations or to run simulations to longer timescales in a computationally efficient manner. Spatial domain decomposition techniques are used to partition or break up the simulation into smaller sub-domains for the distribution to individual processors [30]. However, the ability to increase the number of processor does not necessarily mean that the system of equations will be efficiently solved faster.

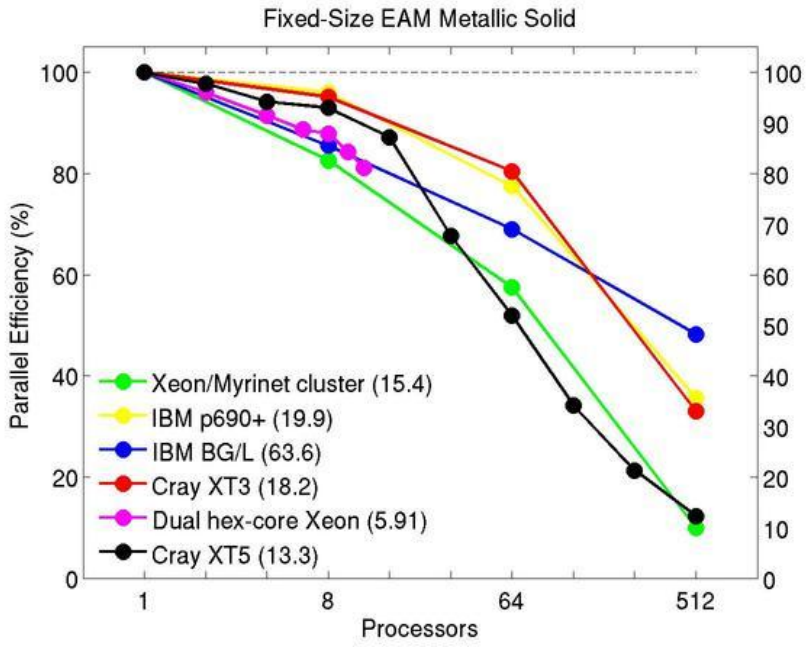


Fig. 2.2 Computational parallel efficiency of the LAMMPS code with increasing number of processors, as reproduced from Ref [33].

Figure 2.2 demonstrates the parallel efficiency of the LAMMPS code as a function of the number of processors for a fixed-size problem, on a variety of high performance computing platforms. Parallel efficiency is defined by the speedup of the simulation divided by the number of processors used. It is clear form Figure 2.2 that an increasing number of processors will enhance the solve time, but will also start to reduce efficiency of the solving capability making the simulation more computationally expensive. LAMMPS is fairly linear in its time stepping, in the sense that each step requires approximately the same amount of time to solve the computational problem. Figure 2.3 shows this linear relationship for a given system.

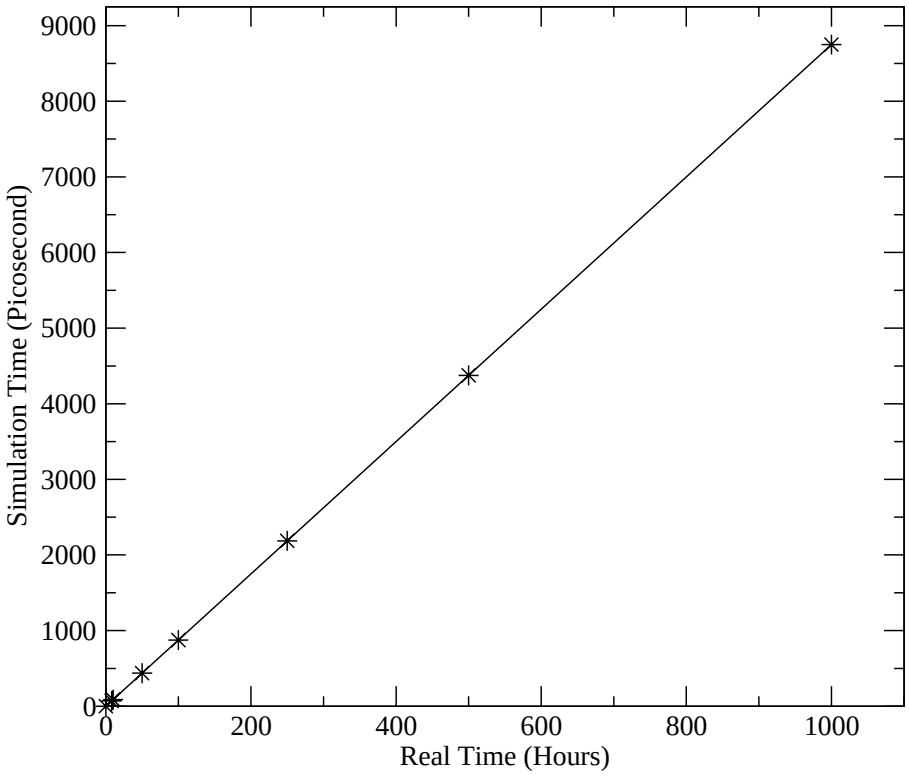


Fig. 2.3 Linear relationship between the amount of simulated time (y-axis) using 8 processors as a function of the wall clock (real time) for a system containing 54000 atoms.

2.3 Interatomic Potentials

An interatomic potential describes the potential energy between two atoms as a function of their distance, which is characteristic for their interaction. A simplified view of this potential energy is given by the Van der Waals interaction describing the attraction between two atoms at larger distances, and the columbic repulsion for smaller distances when the electron orbitals begin to overlap. A traditional Lennard-Jones Potential, which captures these features, is shown in Figure 2.4.

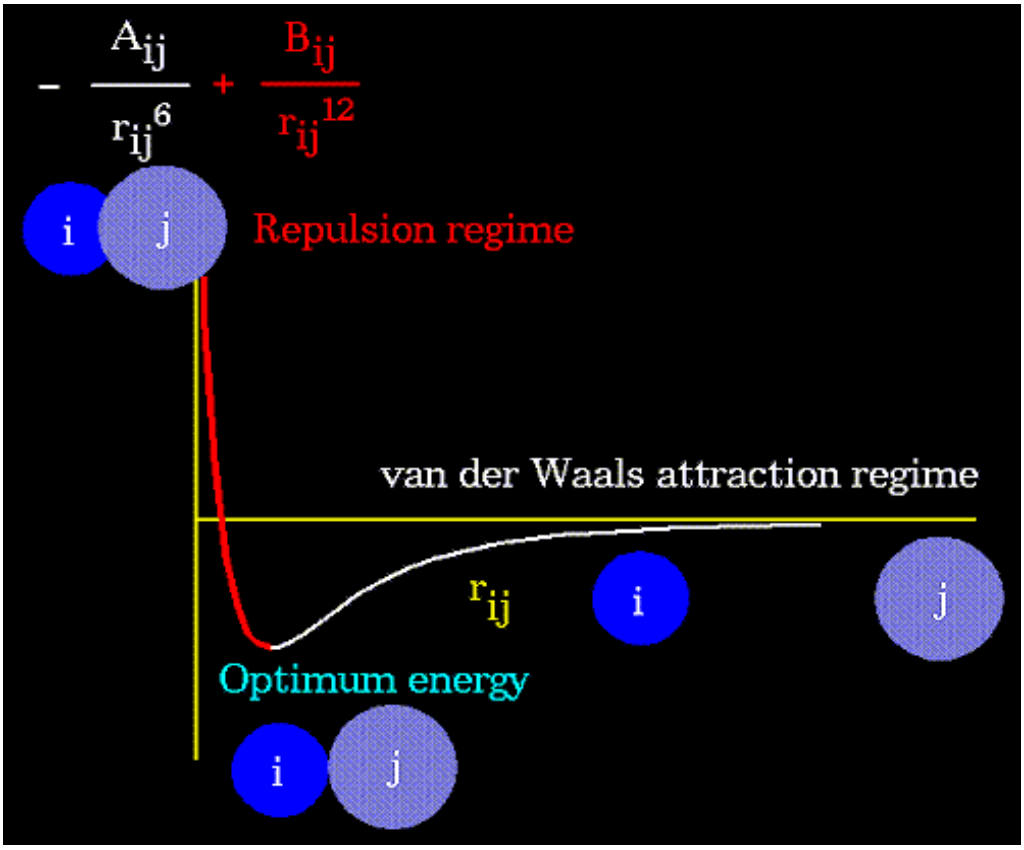


Fig. 2.4 Schematic illustration of a Lennard-Jones potential, as a function of separation distance between a pair of atoms, along with its descriptive equation.

Looking at Figure 2.4, as the two atoms begin to approach each other from an infinite separation they experience an attractive force pulling the two atoms closer together. The Van der Waals force is stronger than the columbic repulsion at this distance, until a minimum energy condition is reached. This minimum energy well represents the lowest energy for the system as well as describes the bond distance (r_{ij}) for these two atoms at 0 K. If one of the two atoms has enough energy for an elastic collision with another atom, the columbic repulsion between the two atoms will begin to dominate the interaction at shorter separation distances. This columbic repulsion regime is a manifestation of the Pauli exclusion principle, prohibiting two particles to occupy the same quantum state at the same time. As the electronic orbitals of two atoms begin to overlap they will exhibit a repulsive force causing them to separate from each other.

For the purpose of the research conducted in the framework of this thesis, three interatomic potentials were used. A pair potential developed by Juslin [34] was used for the Fe-He interactions, the pair potential of Janzen and Aziz [35] was used for the He-He interactions, and an embedded atom model (EAM) potential based on the Finnis and

Sinclair model, developed by Ackland [36], was used for the Fe-Fe interactions.

The Fe-He potential was developed for high energy interactions, where elastic collisions occur. This potential is based on the DMol97 program for the implementation of the columbic repulsion, which was paired with a Van der Waals attractive force [34]. The DMol-potential orbitals are augmented with hydrogen orbitals to calculate the total energy as a function of interatomic distance r [33].The mathematical description of the potential is as follows:

$$f(r_{ij}) = \begin{cases} \text{DMOL-potential}, & r_{ij} \leqslant r_1 \\ p_3 r_{ij}^3 + p_2 r_{ij}^2 + p_1 r_{ij} + p_0, & r_1 \leqslant r_{ij} \leqslant r_2, \\ \left(a + \frac{b}{r_{ij}}\right) e^{-c r_{ij}} f_c(r_{ij}), & r_{ij} \geqslant r_2, \end{cases} \tag{5}$$

where r_{ij} is the distance between atom-i and atom-j, and the cut-off function is:

$$f_c(r_{ij}) = \begin{cases} 1, & r_{ij} \leqslant r_c - r_d, \\ \frac{1}{2}\left(1 - \sin\frac{\pi(r_{ij} - r_c)}{2r_d}\right), & |r_c - r_{ij}| \leqslant r_d, \\ 0, & r_{ij} \geqslant r_c + r_d, \end{cases} \tag{6}$$

The He-He potential is dominated by Van der Waals forces up to very small separation distances, and has a very small interaction energy which is governed by the dispersion energy [35]. The Jazen model is a pair potential, modified from the Tang-Toennies model [35]. The mathematical representation of the potential is as follows:

$$\begin{aligned} V(R) = A\ \exp(-\alpha R + \beta R^2) - \Bigg[1 - \left(\sum_{k=0}^{6} (\delta R)^k / k! \right) \\ \times \exp(-\delta R) \Bigg] C_6 f(R) / R^6 \\ - \sum_{n=4}^{8} \left[1 - \left(\sum_{k=0}^{2n} (\delta R)^k / k! \right) \exp(-\delta R) \right] C_{2n} / R^{2n}, \end{aligned} \tag{7}$$

where R is the displacement from its lattice position.

The Fe-Fe potential is a Finnis and Sinclair N-body potential which is similar to an embedded atom model (EAM) [35]. This potential uses an approximation to describe the potential energy between two iron atoms. Ackland's iron potential is described by:

$$U = \quad {}_i F_i[\quad {}_j \Phi(r_{ij})] + \quad {}_{ij} V(r_{ij}) \tag{8}$$

where the first term is the cohesive function that represents the metallic bonding of the iron, and the second term is a traditional pair interaction function that describes the

screened atomic repulsion at close distances.

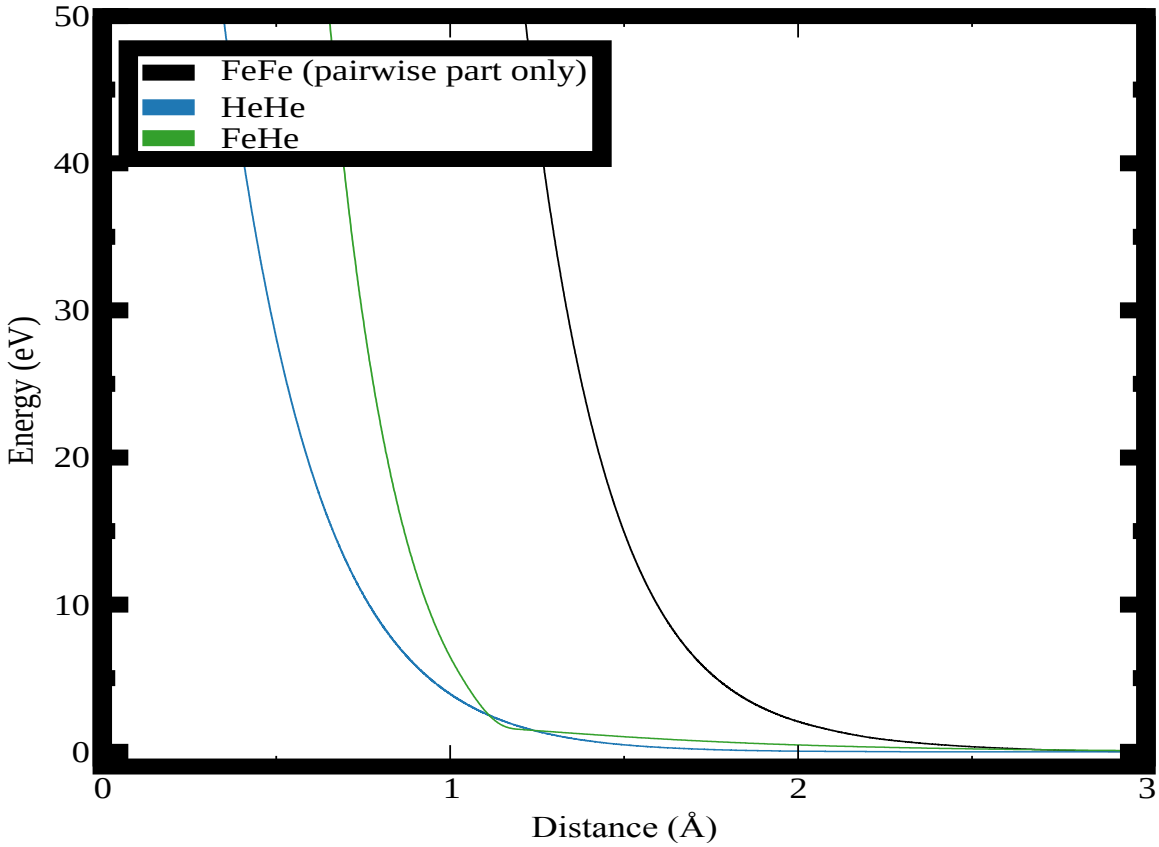


Fig. 2.5 Plot of Potential energy versus separation distance describing the interatomic potential for the Fe-Fe repulsion only (black), He-He (green), and Fe-He (blue).

Figure 2.5 displays the interatomic potentials applied in this thesis as a function of interatomic distance. The He-He and Fe-He potentials are similar to the Lennard-Jones potential with dominating Van der Waals forces at large distances. As the two atoms approach each other, they begin to interact with a repelling force at close distances. The iron-iron potential only represents the pairwise or the repulsive interaction between the two iron atoms. The cohesive function that represents the metallic bonding of the system is not shown since it is a sum of all metallic bonds in the system.

Chapter 3:
Cascade-Loop Interaction

3.1 Methodology

As noted in the introductory chapter, the objective of this study is to evaluate cascade overlap with pre-existing defects. This thesis will evaluate how a cascade would impact a trapped self-interstitial dislocation loop, in terms of both the impact of pre-existing defects on new damage production in the cascade, and the impact of the cascade on the size, morphology, and mobility of the pre-existing defect.

A dislocation loop with 91 self-interstitial atoms was formed and is approximately 2 nanometers in diameter. To trap this dislocation loop, six interstitial helium atoms were distributed along the loop perimeter. The exact nature of the trapping interactions is unknown and may vary from material to material, but in the case of ferritic alloys it is assumed that interstitial impurities such as carbon, nitrogen, and oxygen indeed play a dominant role in this process. Though carbon, nitrogen, and oxygen are most abundant in in practical applications, this computational work used helium as a surrogate due to the simplicity of the interatomic interactions of helium with iron. However, it is important to note that the helium-iron interaction potential used in this work is completely repulsive, and thus it may not be a representative surrogate for more complex chemical interactions of carbon or oxygen interstitial impurities. The dislocation loop was inserted within an otherwise perfect bulk iron crystal with a glide plane in the <111> direction and equilibrated at 300 Kelvin. As previously mentioned, the interatomic interactions were modeled using an embedded atom model (EAM) potential developed by Ackland [37] for Fe-Fe interactions, a pair potential developed by Juslin [35] was used for the Fe-He interactions, and the pair potential of Janzen and Aziz [36] for the He-He interactions.

During the simulation, defects were identified using Lindemann spheres with a radius of 1.01 and 1.81. Atoms not contained within a sphere were labeled as interstitials, while spheres without atoms were labeled as vacancies. The position of the loop was calculated as the center of mass of all identified defects that were part of the loop. The mean squared displacement of the dislocation loop in the glide direction was measured for 10 ns of simulation time at temperatures up to 775 K. In order to identify a fully trapped loop configuration, this process was conducted for loops with either1, 3, or 6 helium atoms distributed in tetrahedral sites at the loop periphery in addition to non-trapped loops without any helium present. Loops without detached helium exhibited glide with an activation energy of 0.044 eV, consistent with previous MD simulations [34]. With a single helium atom near the dislocation, the motion of the loop was suppressed at low temperatures, but the cluster exhibited noticeable co-migration with the helium impurity at higher temperatures, as is shown in figure 3.1. This is similar to the behavior reported for carbon-decorated loops by Topasa [35]. An increase in the number of helium atoms reduced the loop mobility to essentially zero at all temperatures studied. This effect was observed for smaller, 19 member interstitial loops as well.

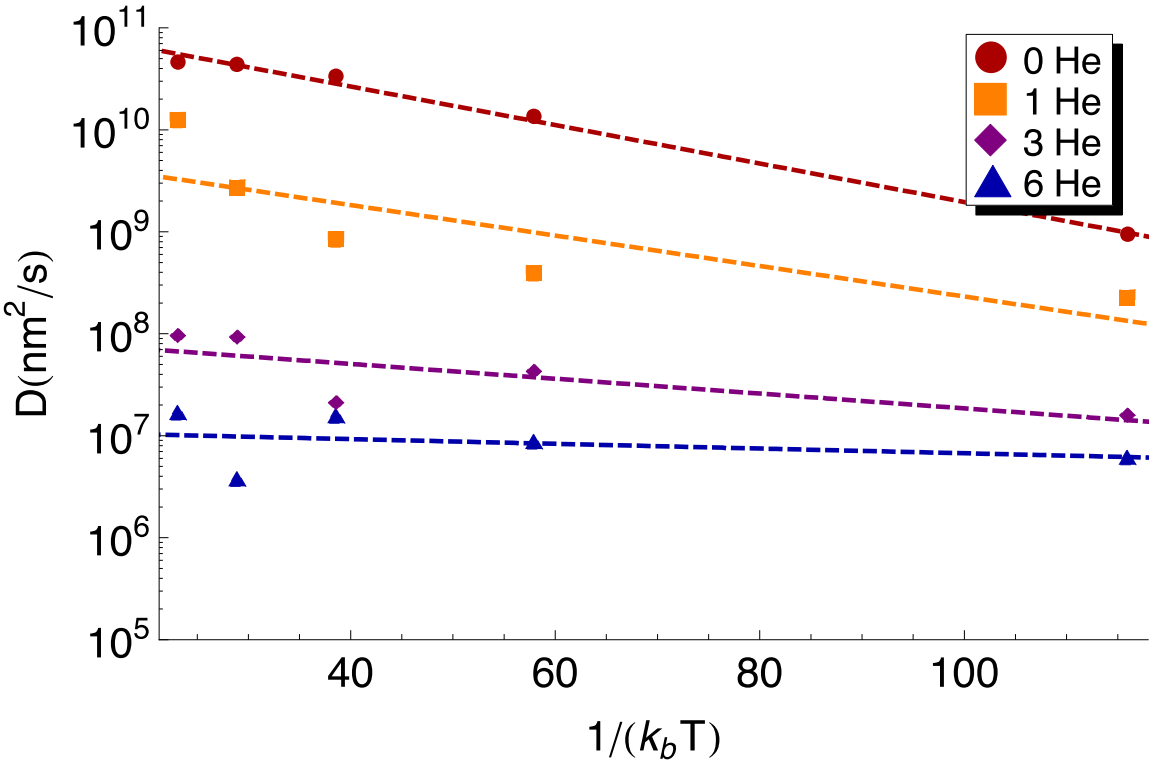


Fig. 3.1 Diffusivity of a 91 member dislocation loop plotted as an Arrhenius relationship for trapped and untrapped dislocation loops, as a function of the number of helium atoms used to trap the loop.

The 91-member dislocation loop, trapped with six helium interstitial atoms, was then inserted into an otherwise perfect bulk iron environment containing from 54000 to 250000 atoms, and equilibrated at 300 K prior to initiating PKAs with varying kinetic energy. Table 3.1 summarizes the different applied PKA energies, along with the cell size of the simulation, and the number of simulations performed for each cascade energy. Three initial PKA energies were chosen to investigate the interaction of the cascade with the trapped dislocation loop. The location and directional velocity of the PKA were different for each simulation, but close enough to the trapped dislocation loop that the cascade could overlap with the trapped loop. A Burgers circuit analysis of the loop was performed after each cascade simulation. A range of starting locations and directions were used to test for internal junctions.

Table 3.1 The system size (number of atoms) used during this study as a function of PKA energy, and the number of cascade simulations performed. All simulations were performed at an initial temperature of 300 Kelvin.

Cascade Energy (keV)	Cell size (number of atoms)	Length of simulation (picoseconds)	Number of simulations
1	54000	70-80	30
5	128000	60-70	30
10	250000	60-70	30

Chapter 3.2 Results

The MD simulations of cascade overlap with a trapped, prismatic interstitial loop revealed a number of possible interactions, including a pressure wave interaction and an affinity of the self-interstitial loop towards the vacancy rich cascade core. The first cascade-loop interaction observed was due to the interaction of the loop with an initial pressure pulse created by the cascade. Figure 3.2 shows the evolution of the cascade and the trapped-loop, where the cascade pressure pulse pushes the dislocation loop free from the helium atoms. In this and subsequent figures, the green spheres correspond to displaced iron atoms, blue spheres corresponds to interstitial helium atoms, and red spheres correspond to vacancies.

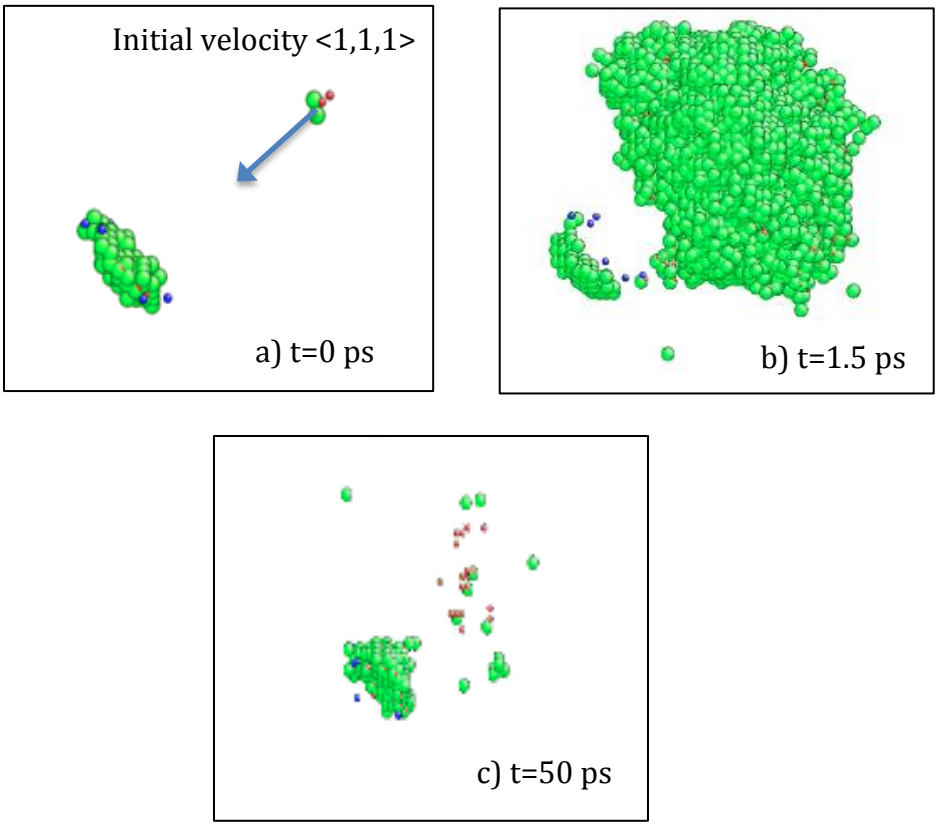


Fig. 3.2 The evolution of a 10 keV cascade near a trapped dislocation loop. The PKA is initially 8.7 nm from the center of mass of the dislocation loop.

During the initial formation of the cascade, a compression wave is produced which can interact with the trapped interstitial dislocation loop. The proximity of the cascade volume and the induced pressure pulse with the trapped dislocation loop is important. The 10 keV cascade shown in Figure 3.2 was initiated at a PKA location shown in Figure 3.2a. The PKA was far enough away from the dislocation loop so that the cascade would not completely encompass the dislocation loop, but close enough for the loop to interact with the compression wave. This initial PKA was 8.7 nm from the loop center of mass. The compression pulse from the cascade was able to push the dislocation loop free from the helium impurities, as shown in Figure 3.2b. As the cascade reaches its peak damage the trapped dislocation loop exhibit a convex shape as the pressure pulse pushes the dislocation loop away from the cascade core. Once the dislocation loop is effectively been dislodged from the helium impurities, it will glide towards the cascade core, where the helium impurities re-trap the dislocation loop. After the dislocation loop is re-trapped, it shows an oscillatory behavior from a concave to a convex shape, while remaining trapped by the helium impurities (Figure 3.2c). It is important to note that a pressure-pulse interaction between the dislocation loop and the cascade was observed for all PKA energies, with the loop being completely de-trapped

from the helium impurities higher cascade energies of 5 and 10 keV. Furthermore, de-trapping was only observed when the bulk of the cascade damage overlapped with the <111> glide prism of the dislocation loop. For the dislocation loops that were de-trapped from the helium, the MD simulations revealed that the helium impurities re-trapped the dislocations loop as it subsequently changed direction and glided back toward the cascade core.

The second and most common cascade-loop interaction occurs after the cascade has reached its peak damage. Following the cascades initial compression wave, it leaves behind a region of low stress creating a tension displacement wave directed back towards the lower density or vacancy rich cascade core. Figure 3.3 shows an example of the dislocation loop interaction with the vacancy rich core of the cascade, which results in complete de-trapping of the loop from the helium atoms.

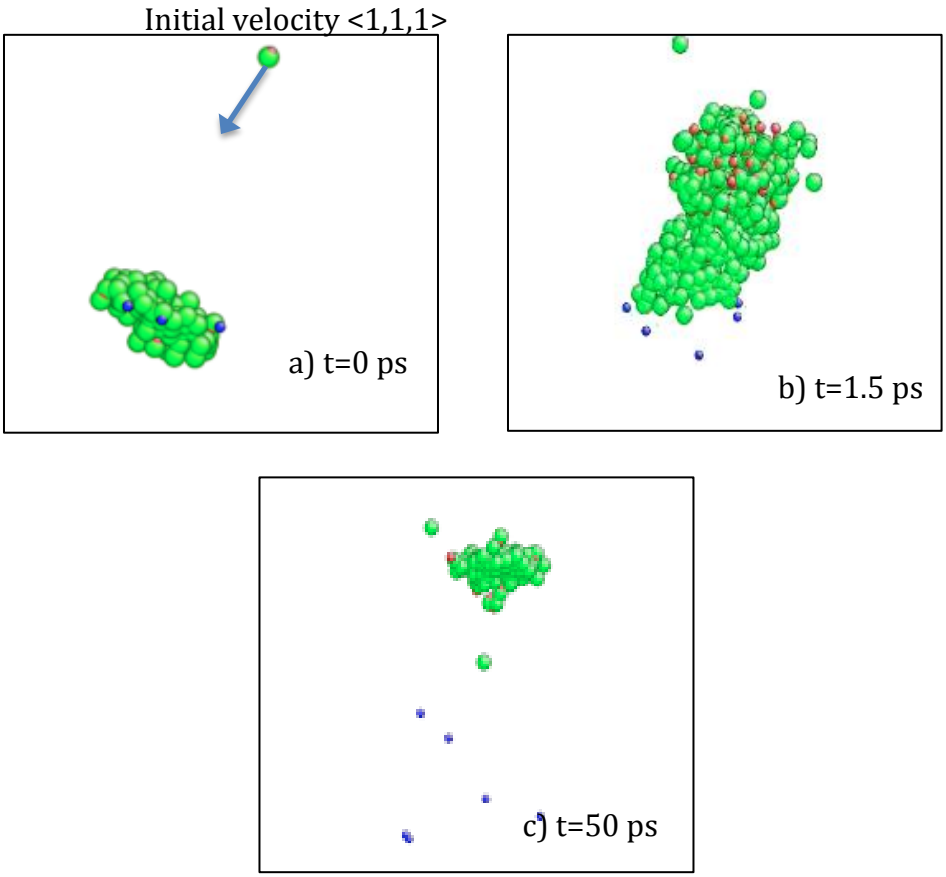


Fig. 3.3 The evolution of a 5 keV cascade that overlaps the trapped dislocation loop, as a function of time. The PKA is initially 2 nm from the dislocation loop center of mass.

Again, initial cascade evolution creates a compressive pressure pulse, which dislodged the dislocation loop from the impurities. After the cascade reached its peak damage, it leaves behind a vacancy rich core. Similar to before, the proximity of the cascade is an important parameter. The example shown in Figure 3.3 is for an initial PKA distance of2 nm from the loop center of mass. The interaction was strongest when the cascade slightly overlapped with the dislocation loop. The vacancy rich core is a low-density region, which induces an attractive interaction with the dislocation loop, producing an affinity to glide toward the core of the cascade. The compressive wave had little impact on the trapped dislocation loop. Figure 3.3b shows the strong affinity of the dislocation loop for the cascade core, and how the dislocation loop glides toward this region. Many simulations revealed that once the trapped dislocation loop was pulled free from the impurities, it was able to remain de-trapped (Figure 3.3 c). This strong interaction between the trapped prismatic loop and the vacancy rich cascade core was apparent for all cascade interactions studied.

Notably, 30 simulations of a 1 keV cascade did not show any evidence of de-trapping of the dislocation loop, whereas for higher PKA energies of 5 and 10 keV a de-trapping was observed. It remains unclear as to how using helium impurities instead of oxygen, nitrogen, or carbon might influence the present simulation results, because of the fast diffusive nature of helium in iron. Furthermore, the cascade was only able to impact the trapped dislocation loop if the bulk of the cascade debris entered the <111> loop direction.

In addition to the potential of de-trapping dislocation loops, a damage cascade can also influence the orientation and size of the loop. At lower PKA energies of 1 and 5 keV, the cascades did not induce rotation of the loop Burgers vector. However in three out of the thirty simulations, a 10 keV cascade did change the orientation of the dislocation loop with its initial <111> direction. As a result of the cascade interaction, three of the thirty initially trapped prismatic dislocation loops contained junctions, with a portion of the loop having a <111> orientation, and the other portion either in the <100> or the <110> direction as shown in Figure 3.4.b. It is unclear whether this junction is thermally stable, or if the dislocation will minimize its energy by orienting into a different Burgers vector direction. However the formation of a <100> dislocation segment provides an interesting possibility associated with the experimental observation of <100> dislocation loops in irradiated ferritic steels which warrants further study.

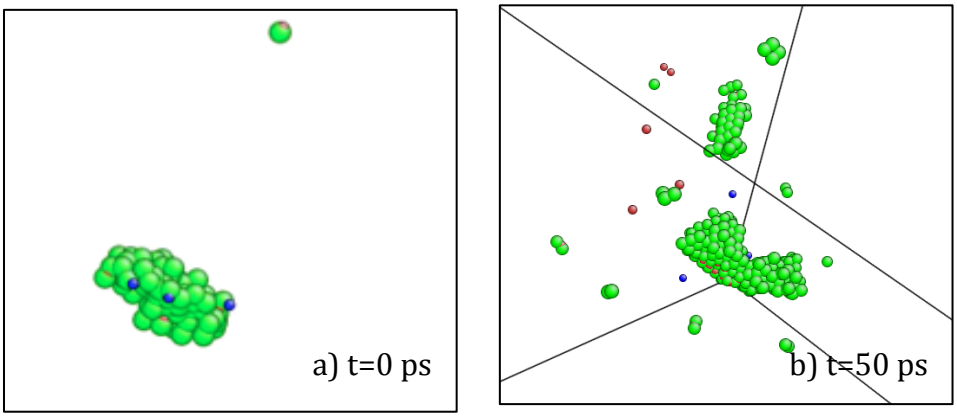


Fig. 3.4 Snapshots in time from a 10 keV cascade, in which a loop formed a junction.

The change in size of the dislocation loop after cascade interactions was determined at the end of each simulation and is summarized in Table 3.2. All cascade simulations were initiated with a starting size of 91 atoms for the trapped dislocation loop. The 1 keV cascade had negligible effect on the average size of the dislocation loop, but as the cascade energy increased the size of the resulting dislocation loop decreased. The 5 keV cascade caused the dislocation loop, on average, to decrease by 6 atoms, and the 10 keV cascade decreased the size of the dislocation loop by 9 atoms. Table 3.2 also indicates the average loop displacement following the cascade event. While 16% of the 5 and 10 keV cascades resulted in de-trapping of the loop, the average loop displacement was quite low indicating that the loop rapidly became trapped again by either the original helium impurities or the cascade damage.

Table 3.2 Quantification of the impact of displacement cascades of the size and mean displacement on the 91-SIA dislocation loop trapped with 6 helium interstitials at 300 K, as a function of PKA energy.

PKA Energy (keV)	Average Final Size of the Dislocation Loop	Standard Deviation (2σ)	Average Loop Displacement (nm)
1	90	1	.075
5	85.3	2.4	.63
10	85	32.1	.302

Table 3.3 Quantification of the impact of displacement cascades on the number of produced Frenkel pairs produced as a function of PKA energy, with a pre-existing 91 member trapped dislocation loop

Energy (keV)	Number of Frenkel Pairs – Dislocation Loop	Standard Deviation (2σ)	SIA Clustering Fraction
1, Perfect Iron	5.51	.37	.25
5, Perfect Iron	13.3	1.4	.3
10, Perfect Iron	23	2.3	.43
1, 91 member trapped loop	2.38	2.2	.14
5, 91 member trapped loop	12.4	9	.3
10, 91 member trapped loop	21.5	35	.4

Table 3.3 provides data on how many defects are produced from each induced cascade. It is clear that the dislocation loop decreased the number of Frenkel pairs produced by the cascade for the 1 keV, and with the addition of the dislocation loop, there is no evident change in the interstitial clustering fraction. Due to the high uncertainty for the 5 and 10 keV simulations, it is difficult to say whether dislocation loop had a significant impact on the number defects produced.

The simulation results clearly indicate that a cascade can induce de-trapping of a dislocation loop from impurities. The first being the final size of the dislocation loop is smaller for all PKA energies, and second the cascade has shown the ability to affect the final orientation of the dislocation loops Burgers vector, primarily for the 10 keV cascades. The cascade influence on loop orientation, and in particular the observation of junction formation needs to be further studied to determine the full impact. Lastly, the pre-existing dislocation loop has caused the number of Frenkel pairs produced by the cascade to decrease.

Chapter 4:

Pre-existing Vacancies effect on defect production

Following the analysis of damage cascade and dislocation loop interaction and its impact on defect production, loop size, orientation, and de-trapping, this chapter describes results of MD simulations of cascade overlap with pre-existing vacancies of different concentrations. This is motivated by cluster dynamic simulations of radiation damage at low temperatures indicating the buildup of unphysically large vacancy concentrations. It is important to address how pre-existing vacancies influence cascade defect production and defect recombination. Related computer simulations must focus on evaluating how the number density of pre-existing vacancies and their spatial distribution may increase the annihilation rate of the damage produced by the cascade.

Using the same methodology as previously discussed for cascade-dislocation loop overlap, cascade simulations were performed with varying PKA energies of 1, 5, or 10 keV in bulk iron with respect to a wide range of pre-existing vacancy concentrations of different spatial distributions. In addition to the randomly distributed vacancies, one set of simulations evaluated also the effect of cascade overlap with voids. Forty unique simulations were performed to improve the statistical accuracy. To build a complete understanding on how pre-existing defects affect the defect production in a cascade, a baseline analysis was conducted using defect free iron simulations for comparison.

The first set of simulations involved clustering all of the pre-existing vacancies into a void. A similar method was used to study how the void would affect the number of Frenkel pairs produced by the cascade. The void was place in the bulk iron with an initial size of 10 and 25 vacancies. Then a cascade was induced with a random position and velocity with the corresponding PKA energy. The simulation ran to a real time of twenty picoseconds. This particular void defect was only analyzed for a 10 keV cascade, but not for the 1 or 5 keV.

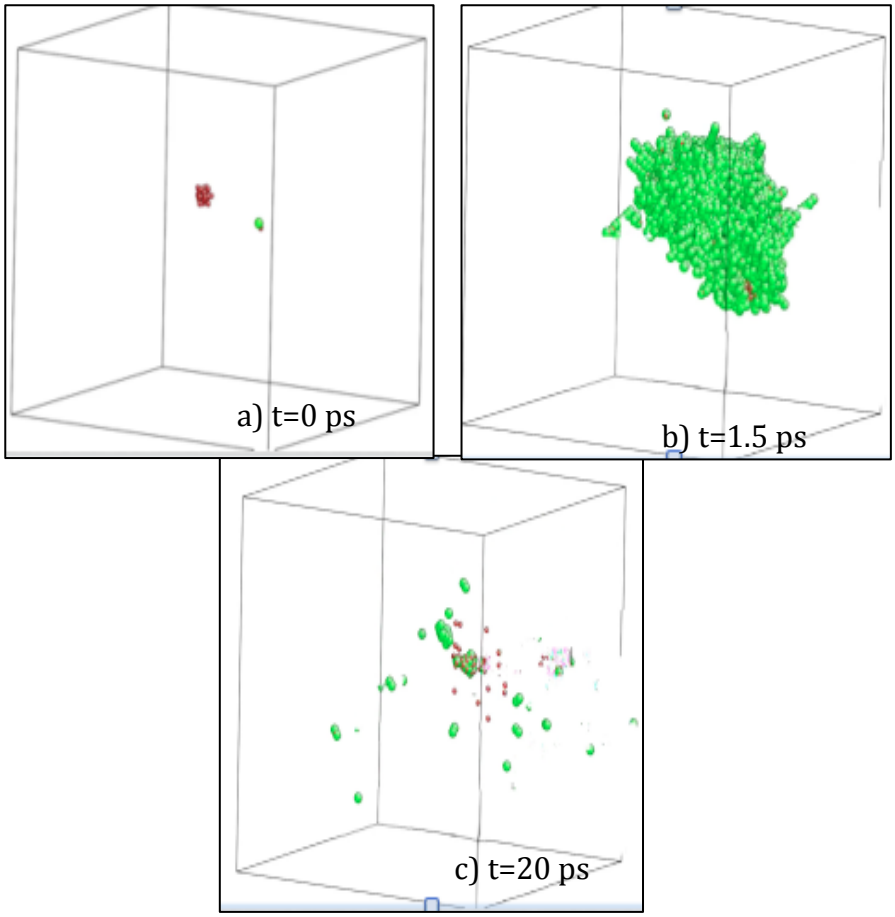


Fig 4.1 Snapshots in time of a 10 keV cascade overlapping with a pre-existing void containing 25 vacancies.

There are a number of different interaction mechanisms that occurred between void and cascade: no cascade-void interaction, cascade interaction with a small portion of the void, or completely engulfed the void. The results of the void impact on defect production are presented in Table 4.1.

Table 4.1 Quantification of the impact of two sizes of voids on the number of Frenkel pairs produced by a cascade with an initial PKA energy of 10 keV.

Material (size V)	Initial Void Size	Final Void Size	Number of Frenkel Pairs Produced	Standard Deviation to 2σ	Difference
Pure Iron	0	0	23	2.3	0
Void (10)	10	8	17.1	1.5	5.9
Void (25)	25	16	17.2	1.7	5.8

It is clear from Table 4.1 that both void sizes have an impact on the number of cascade-induced Frenkel pairs that are produced with a 26% decrease of number of defects produced by a 10 keV PKA in pure iron. Looking at the number of Frenkel pairs produced as a function of initial size of the void shows there is no dependence on the size of the void. The void-cascade interaction resulted also in a reduction of vacancies within the void, with the smaller void experiencing a 20% reduction and the large void experiencing a 34% reduction. This may be related to only a small portion of the peak cascade damage overlaps with the pre-existing void, and therefore changing the initial size of the void would not increase the surface area enough to cause an increase in the overlap interaction between the void and the cascade. By not increasing the void-cascade overlap interaction there would not be a significant change in the number of defects produced by the cascade.

The second set of simulations evaluated the influence of pre-existing defects on a random distribution of vacancies with varying concentrations, as opposed as a single defect. An arbitrary PKA was chosen with a directional velocity corresponding to 1, 5, or 10 keV. Comparing the results of the randomly distributed vacancies to the pre-existing voids, the results are significantly different. Unlike the case where the cascade interacted fully with pre-existing voids, the cascade peak damage interacted only with a small fraction of vacancies. Since the cascade did not interact with all pre-existing vacancies, the number of Frenkel pairs produce by the cascades was higher as compared with the interaction with pre-existing voids. Table 4.2 shows this to be true.

Table 4.2 The influence of the number of pre-existing vacancies on cascade defect production, as a function of vacancy concentration and initial PKA energy.

	1 keV			5 keV			10 keV		
	Frenkel Pairs	Interstitial Clustering Fraction	Standard Deviation (2σ)	Frenkel Pairs	Interstitial Clustering Fraction	Standard Deviation (2σ)	Frenkel Pairs	Interstitial Clustering Fraction	Standard Deviation (2σ)
Defect Free Fe	5.51	.25	.37	13.3	.306	1.4	23	.438	2.3
40 ppm	5.27	.36	.49	13.4	.318	1.4	22	.456	2
100 ppm	5.1	.31	.56	12.9	.33	1.2	20.5	.434	1.7
250 ppm	5.02	.29	.52	12.8	.342	1.2	21.2	.385	2.3
400 ppm	4.6	.26	.41	12.3	.329	1.3	18.6	.376	2

A comparison of the results of the pure iron simulations in Table 4.2 to published data shown in Figure 1.3-1.5, indicates a good agreement with previous studies. By adding pre-existing vacancies with increasing concentration increases cascade overlap, and increases in self interstitial atom-vacancy annihilation reactions occurs, which decreases the number of Frenkel pairs produced. As presented in Table 4.2, the trend of increasing vacancy concentration produces a decrease in the number of defects produced in a cascade. This trend was expected because the increase in vacancies leads to more available locations for SIA-vacancy annihilation to occur. Furthermore these results are summarized in Figure 4.2, which plots the ratio of defects produced in a material as a function of vacancy concentration divided by the number of defects produced in pure iron, as a function of PKA energy.

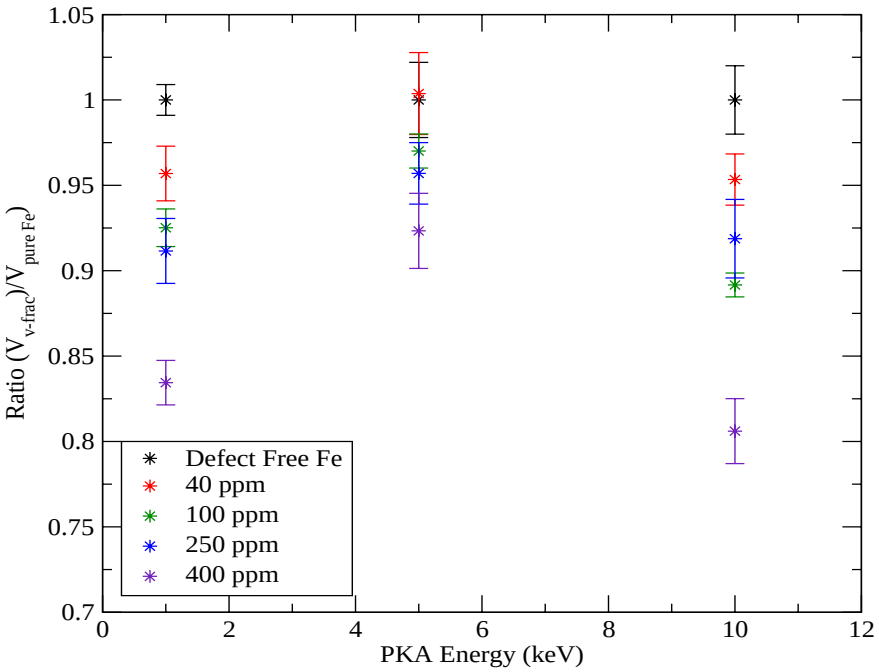


Fig 4.2 The effect of pre-existing vacancies on defect production in displacement cascades, as a function of PKA energy and vacancy concentration. The ratio is the number defects produced with randomly distributed vacancy concentration present relative to the number of defects produced in pure iron.

As seen in Figure 4.2, it is evident that pre-existing vacancies will have a significant impact on the number of defects that are produced by the cascade for larger vacancy concentrations. Figure 4.2 relates the number of Frenkel pairs produce in a material with the concentration of vacancies in comparison to a defect free or pure material. The impact that the pre-existing vacancies have on the defect production ranges

from, in the smallest case for a vacancy concentration of 40ppm, deviating 1% from the number of defects in pure material. Where the largest case having a vacancy concentration of 400ppm decreasing the number of defects produced by ~20%. It is unclear why the simulations with a 5 keV PKA do not exhibit a similar change in defect production as compared to the 1 and 10 keV PKA's. A possible explanation for this modified behavior may be related to the size of the simulation box, which might have been too small for the cascade. If the simulation box is too small the interaction of the cascade with itself or with vacancies may be lower as compared with larger simulation boxes. This would result in a decrease in annihilation interactions.

Another interesting point is how the pre-existing vacancies impacted the self-interstitial clustering fraction as a function of vacancy concentration and PKA energy. Figure 4.3 evaluates the impact the pre-existing vacancies had on the SIA clustering fraction.

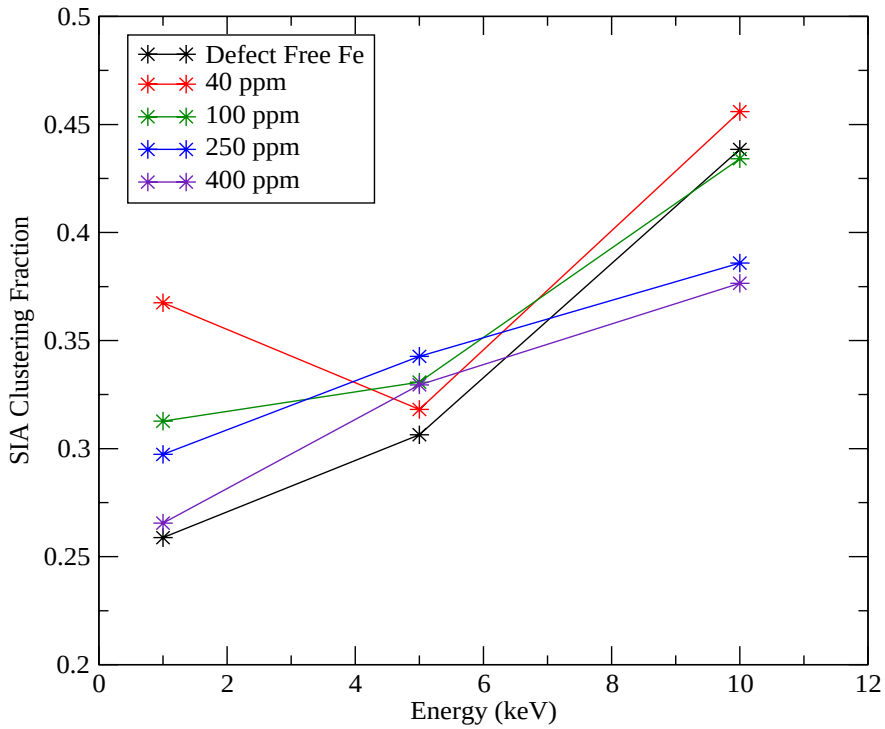


Fig 4.3 The self-interstitial clustering fraction observed as a function of PKA energy and concentration of pre-existing vacancies.

It is evident that the pre-existing vacancies increase the SIA clustering fraction, as shown in Figure 4.3. As the cascade begins to create damage in the material there are many types of defects induced with the majority of single interstitials. The presence of pre-existing mono-vacancies in the material will lead to annihilation with many single interstitials.

The presence of pre-existing defects has a significant impact on the number of Frenkel pairs that are produced by an induced cascade. This is seen by the percentage of the defect produced by the cascade decreasing by 5-20% with increasing vacancy concentration. Furthermore, the percentage of self-interstitial clusters formed during the cascade increases with increasing vacancy concentration, for the majority of cases. This gives evidence that the damage not only is decreasing in numbers, but that the surviving damage tends to remain in the form of small interstitial clusters more frequently. Lastly, an analysis of the effect of void overlap with a cascade has shown a significant effect on how many Frenkel pairs are produced by the cascade, independent of the voids size.

Chapter 5:
Summary and Outstanding Issues

Molecular dynamics simulations have been performed to study the affect of pre-existing defects on the evolution of displacement cascades in close proximity with the defects, as well as the influence of the defects on defect production. Cascades induce complete de-trapping of dislocation loops from helium impurities 16% of the time for a PKA energy of 5 or 10 keV. The most common outcome was the dislocation loop initially de-trapped but subsequently re-trapped 40% of the time, for all PKA energies. It is unclear if this was due to the fast diffusive nature of helium in iron or the distance the dislocation loop was pulled or pushed away from the impurities during the de-trapping event. Overall, the overlap of a cascade separated the dislocation loop from the trapping helium impurities 56% of the time. The dislocation loop exhibited a strong affinity for the vacancy rich cascade core. The vacancy rich core, which was produced by only PKAs of energy of 5 or 10 keV, interacted with the loop resulting in annihilation reactions that effectively decreased the loop size. Furthermore, lower PKA energies, 1 or 5 keV, did not influence the dislocation loops Burgers vector; whereas the 10 keV PKA caused a change in orientation of the Burgers vector and created junctions in the dislocation loop following the cascade. 34% of the cascade simulations did not affect the loop size, morphology or trapping at all.

The affect of pre-existing vacancies on cascade defect production was significant. The type, as well as the concentration of, pre-existing vacancies had a significant impact on the number of defects produced. Simulations containing a void had a large impact on the number of defects produced, but changing the initial void size form 10 to 25 vacancies did not change the affect on defect production relative to a cascade in defect-free iron. Randomly distributed vacancies had a non-saturating affect on the amount of defects produced in a cascade. As the concentration of pre-existing vacancies increased, the number of Frenkel pairs produced decreased. The presence of randomly distributed vacancies also produced an increase in the fraction of interstitials in clusters. This trend indicates that SIA clustering fraction increases as the concentration of randomly distributed pre-existing vacancies increased.

Many question remain to be fully answered. The first is to improve the statistical certainty of how the size of the 91 member dislocation loop will change following a 10 keV cascade. Also the observation of a dislocation loop containing a junction following interaction with a cascade needs to be better understood by either performing longer MD simulations or by simulating the dislocation loop using kinetic Monte Carlo to extend to longer timescales. Furthermore, to fully understand how a dislocation loop is de-trapped from impurities in a material, future simulations should investigate carbon, nitrogen or oxygen as the trapping impurities to understand how chemical interactions will influence loop trapping and de-trapping behavior, in addition to the elastic interactions between helium impurities studied in this thesis.

List of References

[1] Z. Yao et al, Phil. Mag. 88 (2008) 2851
[2] C. Björkas, K. Nordlund, L. Malerba, D. Terentyev, Pär Olsson, J. Nucl. Mater 312-317 (2008) 372
[3] I.M. Robertson, M.L. Jenkins, and C.A. English, J. Nucl. Mater. 108 (1982) 209
[4] S. Xu, Z. Yao, M.L. Jenkins, J. Nucl. Mater. 386 (2009) 161
[5] R.E. Stoller. (2012) Primary Radiation Damage Formation. Comprehensive Nuclear Materials, volume 1, pp. 293-330
[6] T. Hamaoka, Y. Satoh, H.Matsui, J. Nucl. Mater. 433 (2013) 180
[7] I.M. Robertson, M.A. Kirk and W.E. King, Scripta Metall. 317 (1984) p.18.
[8] K. Arakawa H. Mori, and K. Ono 307 (2002) 272
[9]M. Eldrup, B.N. Singh, S.J. Zinkle, T.S. Byun, K. Farrell, J. Nucl. Mater, 2002, 307, 912-917
[10] R.S. Averback, T. Diaz de la Rubia, R. Benedek Nucl. Instrum. Meth. B, 33 (1988), p. 693
[11] A.F. Calder, D.J. Bacon J. Nucl. Mater., 207 (1993), p. 25
[12] R. E. Stoller, J. Nucl. Mater 233–237 (1996) 999
[13] Malerba, L. J. Nucl. Mater. 2006, 351, 28-38
[14] Bacon, D. J.; Osetsky, Yu. N.; Stoller, R. E.; Voskoboinikov, R. E. J. Nucl. Mater. 2003, 323, 152–162.
[15] L. Malerba et al. / Journal of Nuclear Materials 406 (2010) 19–38
[16] D. Terentyev et al. / Journal of Nuclear Materials 351 (2006) 65–77
[17] C. Bjorkas, K. Nordlund/Nucl. Instr. and Meth. in Phys. Res. B 259 (2007) 853–860
[18] R.E. Stoller, G.R. Odette, and B.W. Wirth, J. Nucl. Mater. 251 (1997) 49
[19] L. Malerba, J. Nucl. Mater. 351 (2006) 28
[20] W.J. Phythian, R.E. Stoller, A.J.E. Foreman, A.F. Calder, D.J. Bacon, J. Nucl. Mater. 223 (1995) 245
[21] R.S. Averback, T. Diaz de la Rubia, Solid State Phys. 51 (1998) 281.
[22] C.S. Becquart et al, J. Nucl. Mater. 351 (2006) 39
[23] A. Souidi et al, J. Nucl. Mater 355 (2006) 89
[24] Yu. N. Osetsky et al, Phil. Mag. 83 (2003) 61
[25] B.D. Wirth et al, J. Nucl. Mater 276 (2000) 33
[26] B.D. Wirth, V. Bulatov, T. Diaz de la Rubia, J. Nucl. Mater. 283-287 (2000) 773
[27] D. Terentyev, L.Malerba, and A. V. Barashev Phil. Mag. 88 (2008) 21-29
[28]j. Marian, B. D. Wirth J Perlado, G. R. Odette, and T. Diaz, MRS Proceedings, 650
[29] K. Arakawa et al, Science 318 (2007) 956
[30] Jaime Marian, Brian D. Wirth, Robin Schäublin, G.R. Odette, J.Manuel Perlado, J. Nucl. Mater. 323 (2003) 181
[31] D. J. Bacon and T. Diaz de la Rubia, J. Nucl. Mater. **216**, 275 (1994)
[32] LAMMPS. Available from: http://lammps.sandia.gov
[33] N. Juslin and K. Nordlund, J. Nucl. Mater. 382 (2008) 143
[34] A.R. Janzen and R.A. Aziz, J. Chem. Phys. 107 (1997) 914
[35] G. J. Ackland, M. I. Mendelev, D. J. Srolovitz, S. Han and A. V. Barashev, J. Physics: Condensed Matter, 16 (2004) S2629
[36] B. D. Wirth, G. R. Odette, D. Maroudas, G. E. Lucas, J. Nucl. Mater. **276**, 33 (2000)
[37] K. Tapasa et al, J. Nucl. Mater. 361 (2007) 52

Vita

Nathan Allen Capps was born in Fort Smith, Ar to the parents of Barbara and Thomas Capps. He attended Van Buren High School, where he was a two year varsity starter in football and a three year starter in baseball. He attended the University of Arkansas at Fort Smith, where he played baseball for a year and a half. Upon transferring to the University of Tennessee at Knoxville, he earned a Bachelor of Science degree in Nuclear Engineering in May of 2012. He accepted a Graduate Research Assistant position within the Nuclear Engineering Department at the University of Tennessee upon graduation in 2012. Nathan will earn a Master of Science degree in Nuclear Engineering in December of 2013, and continue his studies for a Doctorate in Nuclear Engineering.